

# The response of metal-matrix composites subjected to quasi-static and shock-wave deformation

J. C. Huang and Y.-S. Lo

*Institute of Materials Science, National Sun Yat-Sen University, Kaohsiung (Taiwan, ROC)*

G. T. Gray III

*Los Alamos National Laboratory, Los Alamos, NM 87545 (USA)*

(Received September 25, 1992; accepted January 4, 1993)

## Abstract

The mechanical response and substructure evolution of three composites (Al–Li alloy reinforced with 55 vol.% Al<sub>2</sub>O<sub>3</sub> long fibers, P/M aluminium alloy X7091 reinforced with 30 vol.% B<sub>4</sub>C particulates, and Ti–6Al–4V alloy reinforced with 42 vol.% B<sub>4</sub>C-coated B long fibers) subjected to shock loading (strain rate > 10<sup>6</sup> s<sup>-1</sup>) and quasi-static compression or tension (strain rate ≈ 10<sup>-3</sup> s<sup>-1</sup>) were examined. The as-received materials were first characterized in terms of both the phase identification of the interfacial reaction products and the measurement of basic low-rate mechanical properties. The materials were shock-loaded using a gas launcher to a peak shock pressure of nominally 5 GPa. Post-shock reload tests at quasi-static strain rates were then applied to the shock prestrained composites in order to trace the mechanical response due to shock loading. The dynamic deformation behavior was compared to that during quasi-static deformation. The results showed that the passage of a shock wave can produce appreciable damage to composites, especially for fiber-reinforced materials. This damage is attributed to the fact that tensile waves are induced whenever the shock wave encounters a ceramic/metal interface in a composite, owing to the shock impedance mismatch. Finally, the substructure evolution and deformation/fracture behavior of the composites after dynamic and quasi-static loading are compared and discussed in light of single-phase material response to shock-loading.

## 1. Introduction

In recent years there has been increased industrial interest, particularly for aerospace and defense applications, in the deformation response of metal-matrix composites (MMCs). Early studies on MMCs addressed the development and behavior of continuous fiber reinforced materials. More recently, discontinuously reinforced MMCs, including both particulates and short whiskers, have attracted considerable attention as a result of the availability of various types of reinforcements at competitive costs and the successful development of manufacturing processes to produce various MMCs. The type of reinforcement is known to play a significant role in controlling the mechanical properties of composites such as toughness. For example, particulate reinforced materials generally exhibit greater toughness than those reinforced with fibers or whiskers [1].

Although the mechanical response of various MMCs has previously been studied, their response under high-rate or impact loading has not been widely explored.

Most of the studies on MMCs have been limited to quasi-static strain rates and most often used tension tests. Future utilization of these composites for some aircraft applications requires that they have sufficient strength and toughness under both conventional and high-rate/impact deformation. The latter is of concern when the airplane is subjected accidentally to an impact or shock wave during service, either in the air (e.g., heavy weather or unexpected collision by some object, referred to as foreign object damage (FOD)) or on the ground (e.g., an explosive-driven wave). Questions requiring further investigation include whether MMCs are strain rate sensitive, how and if the quasi-static properties of MMCs can be applied to their design under impact or shock loading, and how the properties of MMCs are altered following a shock/impact event.

Previous studies of high-rate loading on metals or polymer-base composites [2–5] have suggested caution in attempting to predict the post-shock response of complex materials. It has been noted that a number of internal defects may be introduced during high-rate/shock loading, and the propensity and distribution of

these defects depend on the loading velocity, loading pressure, projectile size and shape, and composite properties (especially the interface nature) [2]. From previous shock-loading experiments [6] it is known that release waves can be anticipated wherever the shock or impact compressive wave encounters and interface between two distinct constituents (owing to impedance mismatches), such as the interface between the matrix and reinforcement or even two semi-bonded laminates of similar materials. This rarefaction wave can result in local debonding failure within a composite. Since the mechanical properties of composites are closely related to interfacial properties, appreciable influence on the subsequent post-impact performance due to these structure degradations is expected.

It should be noted that the internal damage generated in composites by controlled 1-D shock loading will often not be readily apparent macroscopically after the shock. The transient deformation that occurs during shock or impact loading at modest shock pressures is localized within a small volume at one time as it sweeps through a material, i.e., when the shock wave front is located at the middle layer of the sample, the front and rear layers remain inertially disconnected. Accordingly, the deforming layer will experience the constraint from other portions of the specimen and cannot deform freely or plastically as a bulk sample. The residual strain after well-controlled 1-D shock or impact loading is usually very low or undetectable, although severe internal damage and local plastic deformation have already been induced. This is because a residual strain of 1–2% may be measured in a well shock-recovered sample subjected to a modest shock-loading excursion while the corresponding dynamic transient strain was perhaps as high as 20%.

The purpose of the current study was to explore the influence of loading rate and orientation on the structure/property response of several composite materials. The study focuses in particular on the deformation modes and substructure evolution in several MMCs with different reinforcement morphologies subjected to shock loading. The question of how the reinforcement (plus interfacial products) interacts with the matrix during high-rate deformation is of special interest. Various forms and types of reinforcements and matrices in the composites were chosen, so that a more general picture of the mechanical response of composites could be traced. This paper reports results on the tensile and/or compressive deformation of composites following high-rate shock ( $\dot{\epsilon} \approx 10^6$ – $10^8$  s<sup>-1</sup>) and quasi-static ( $10^{-3}$  s<sup>-1</sup>) loading. Results on composite response at intermediate rates ( $10^2$ – $10^4$  s<sup>-1</sup>) and Charpy impact will be presented elsewhere.

## 2. Experimental

### 2.1. Materials

The materials selected were Al–Li/Al<sub>2</sub>O<sub>3(f)</sub>, 7091Al/B<sub>4</sub>C<sub>(p)</sub>, and Ti–6Al–4V/B<sub>4</sub>C/B<sub>(f)</sub> systems. The Al–2.5 wt.% Li/55 vol.% Al<sub>2</sub>O<sub>3</sub> composite was fabricated by DuPont and was obtained in rod form, approximately 7×7 mm in cross section. The aluminium matrix contained 2.5% lithium in order to promote wetting between the fibers and the matrix. The alumina fibers were ≈ 20 μm in diameter, with a polycrystalline structure characterized by a ≈ 0.5 μm grain size. Alumina fibers offer the potential advantages of low cost, environmental stability and compatibility with a number of aluminium alloys. The liquid metal vacuum infiltration technique was used to prepare this composite [7, 8]. As the first step, an α-Al<sub>2</sub>O<sub>3</sub> fiber tape was prepared using a fugitive binder in a manner similar to that used to produce a resin matrix composite prepreg. FP fiber tapes were then laid up in the desired orientation to define the desired preform and molten Al–Li alloys injected into the preheated fiber-preform at 650 °C.

A powder metallurgy (P/M) processed 7091 aluminium reinforced with 30 vol.% B<sub>4</sub>C particulates (≈ 5 μm) was obtained from Lockheed in the form of a thick plate with a thickness of ≈ 10 mm. X7091 is a member of the aluminium alloy family designed for the P/M process. The current composite was prepared by the press-and-sinter powder metallurgy method, where the powders were blended, compacted, degassed, sintered and hot isostatically pressed to full density. The chemical composition of the P/M 7091Al alloy is listed in Table 1. The higher Co-content in the P/M 7091Al alloy is known to result in higher strength and stress corrosion crack resistance than ingot metallurgy (I/M) produced 7075 and 7050 Al. The standard T6 treatment for the 7091 alloy was applied to this composite.

The Ti-base composite was provided in the form of a thin sheet approximately 1.2 mm thick, and consisted of six plies of Ti–6Al–4V with 42 vol.% unidirectional long fibers. The fibers used were nominally 140 μm in diameter and were B<sub>4</sub>C coated B. The B<sub>4</sub>C layer, which was coated onto the B fibers by chemical vapor deposition, was considered to be crucial to fiber properties, since it may act as a diffusion barrier to minimize deleterious reactions with the matrix and thus act to preserve fiber strength [9]. The as-received composite was heat-treated at 950 °C for 30 min. In order to

TABLE 1. The measured chemical composition of the P/M 7091 Al matrix alloy (in wt.%)

Si	Fe	Cu	Mg	Zn	Co	O	Others	Al
0.12	0.15	1.5	2.5	6.5	0.4	0.35	0.15	bal.

satisfy the shock-loading sample requirements, three layers of the Ti composites were stacked together to a total thickness of 3.6 mm.

## 2.2. High-rate shock-loading experiments

Cylindrical specimens (15–20 mm in diameter and 3–3.6 mm thick) of the composites were shock-loaded, with the shock wave travelling through the thickness of the sample. In the case of Ti-6Al-4V/B<sub>4</sub>C/B composite, the shock was perpendicular to the fiber direction, in contrast to the Al-Li/Al<sub>2</sub>O<sub>3</sub> composite, where the shock was applied parallel to the fiber direction. The shock specimen assembly was tightly placed into a similarly sized bored recess in the inner momentum ring/spall plate (44.4 mm in diameter). This central cylinder, in turn, was surrounded by two concentric momentum trapping rings with outside diameters of 69.8 and 82.5 mm. The sample surfaces were protected from impact and the entire sample from spallation by a close-fitting cover plate (2.54 mm thick) and spall plate support (10 mm thick), respectively. All assembly components were made of 6061-T6 Al or Ti-6Al-4V, for the aluminum and titanium composite, respectively, to ensure good impedance matching during shock loading. The sample assembly was placed in a steel impact cylinder that allowed passage of the sample/inner momentum ring through a central hole but stopped the projectile. The samples were soft recovered and simultaneously cooled by decelerating the sample/inner momentum ring in a water catch chamber positioned immediately behind the impact surface. All of the above designs were necessary to prevent sample bending or distortion during shock loading. Other details of the shock experiment have been presented elsewhere [4]. The composite samples were shocked to  $\approx 5$  GPa for 1  $\mu$ s pulse duration through the impact of a 3.0-mm-thick 6061-T6 Al or Ti-6Al-4V flyer plate, for the aluminum and titanium assemblies, respectively, fixed to a projectile filled with low impedance glass microballoons. Impact velocities were 525 and 640 m s<sup>-1</sup> for the aluminum and titanium composites, respectively, to achieve a nominal 5 GPa peak shock pressure level. These velocities represent symmetric-impact calculated peak pressures based on the equation of state (EOS) of the monolithic metals. Exact peak pressures are currently difficult or impossible to predict in composites because of: (1) a lack of measured EOS data on most composites; (2) the breakdown in our ability to calculate an EOS using the previously developed ‘rule of mixture’ owing to the high volume fraction and anisotropy of the second phase distribution; and (3) our current lack of calculational and physical modeling predictive capability to address wave dispersion effects on EOS in multi-component anisotropic materials. The nominal shock transient strain for a 5 GPa shock, defined as

$4/3[\ln(v/v_0)]$ , where  $v$  and  $v_0$  are the shock-compressed and initial volume of the sample, was calculated to be  $\approx 7$ –9% for all three metal-matrix composites. The true strain in the reinforcing ceramics is currently impossible to calculate, owing to the lack of sufficient Hugoniot data and composite wave mechanics. All the recovered composites were flat and possessed measured residual strains of 1–2%, typical of a well-momentum-trapped shock assembly [4]. One-half of each shock-loaded specimen was cut into slices from which samples for transmission electron microscopy (TEM) were prepared. Small cylindrical compression or flat tensile specimens for post-shock reload stress–strain measurements were electron-discharge machined (EDM) from the remaining half (Fig. 1).

## 2.3. Quasi-static tests on the as-received and shock-prestrained samples

Compression and/or tension tests were conducted at room temperature with a conventional screw driven Instron machine at a strain rate of  $10^{-3}$  s<sup>-1</sup> for both the as-received (AR) and shock-prestrained (SP) samples. Since the SP specimens have to be machined from the shock-loaded samples, they are all subsized specimens. The cylindrical compression specimens (AR and SP) were 2 mm in diameter and 2 mm long, while the tensile specimens (AR and SP) were 1.1 mm thick, 3 mm wide, and 5 mm in gauge length. This sample size (hereafter referred to as the ‘tiny’ sample) does not satisfy the ASTM standards for mechanical test samples. Therefore, only a relative, qualitative comparison between the AR and SP samples will be made. The reload flow strength quoted is an average value of three tests. In contrast to homogeneous and isotropic materials, measurement of the compressive strength of the composites was difficult and the results tended to be highly dependent on the loading geometry and testing conditions. The main problem in using such small fiber-reinforced composite specimens was the difficulty in

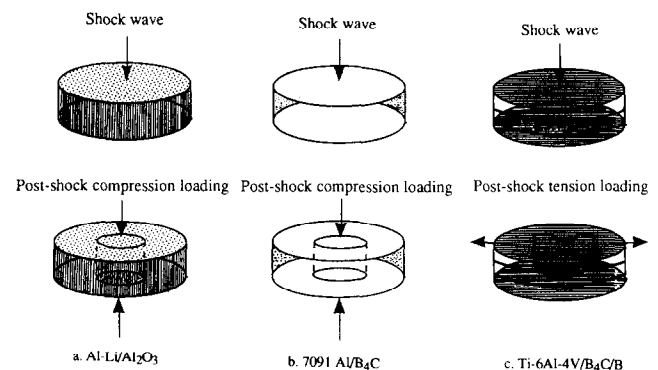


Fig. 1. Schematic illustration of the orientations of the shock-loading and post-shock reload tests for the three composites.

obtaining good sample alignment and ensuring a valid measurement without premature failure.

In addition, in order to characterize the mechanical properties of the composites in a more meaningful manner, larger quasi-static tensile and compression samples, close to the ASTM requirements, were also prepared and tested. These experiments were conducted at a strain rate of  $10^{-3} \text{ s}^{-1}$ .

#### 2.4. Optical and electron microscopy

Samples for TEM were sectioned from the as-received and shock-loaded bulk specimens for all the composites. Specimens were prepared by sectioning, disk-cutting, mechanical grinding, dimpling and ion milling. Most of the ion milling of the composites was conducted using a cold stage. Observation of the TEM foils was done with a JEOL 200CX operated at 200 kV with a double tilt stage. Optical microscopy (OM) and scanning electron microscopy (SEM) were done to characterize the fracture surfaces and interface regions between the reinforcements and the matrix. The etchant reagents for the OM and SEM Al composite samples consisted of 4 ml HF, 6 ml HCl, 20 ml  $\text{HNO}_3$  and 370 ml dilute water. No reagent was used for the Ti composite, since the B fibers were much larger in diameter and were easier to see without etching.

### 3. Results and interpretation

#### 3.1. Characterization of the as-received composites

##### 3.1.1. General microstructural characterization and reaction product identification

*Al-Li/Al<sub>2</sub>O<sub>3</sub>( $\phi$ )*. A typical SEM micrograph of the AR Al-Li/Al<sub>2</sub>O<sub>3</sub> composite is shown in Fig. 2(a). Fibers are seen to be randomly distributed in the matrix. It can be seen that there is an interaction zone between the reinforcement and the matrix. Significant fiber-matrix reaction occurs during fabrication by the liquid metal vacuum infiltration process, and this result is consistent with that seen by Majidi and Chou [10]. The reaction zone was observed to be approximately 2  $\mu\text{m}$  thick in the as-received condition, and there were no precipitates or inclusions at the interface, as shown in Fig. 2(b). Intrinsic defects (pores) within the Al<sub>2</sub>O<sub>3</sub> fibers were also seen. These are postulated to affect the failure behavior of the composite. Analysis of diffraction patterns from the Al-Li matrix region indicated that the metastable  $\delta'$  (Al<sub>3</sub>Li) phase was not present. It appears that most of the Li atoms have contributed to the formation of fiber/matrix interfacial reaction products and thus did not simultaneously allow the nucleation of the  $\delta'$  phase.

Lithium is believed to reduce alumina, thus causing the grayish color of the interfacial reaction products in the composite. Careful measurements of the  $d$ -spacing

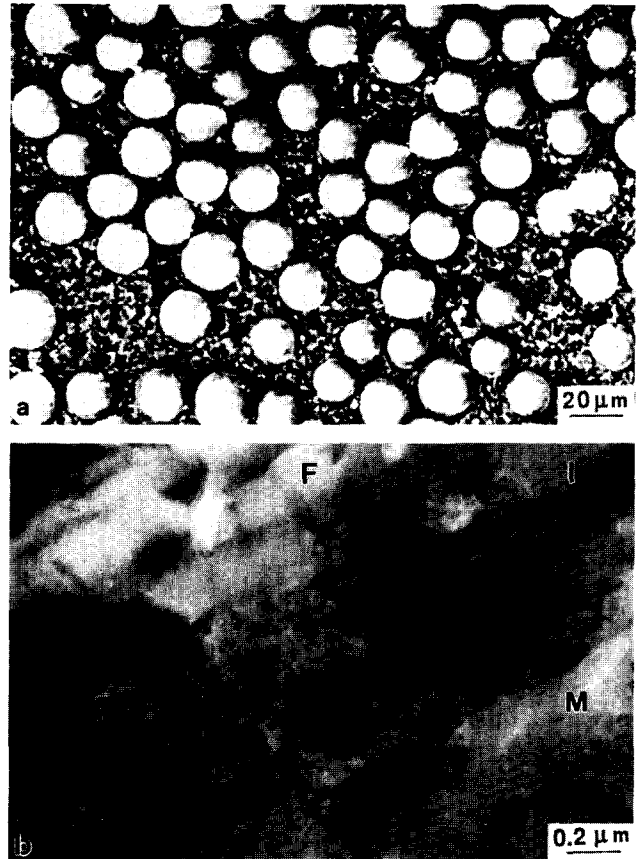


Fig. 2. (a) SEM micrograph of the polished and etched microstructure, and (b) TEM micrograph of the interface region in the Al-Li/Al<sub>2</sub>O<sub>3</sub> composite. The fiber, interface and matrix are marked F, I and M, respectively.

of the reaction products from the electron diffraction patterns were performed. The measured  $d$ -spacing values were compared with the data cards for Al/Li/O compounds in the JCPDS Powder Diffraction Files, and good correspondence was found with the  $\alpha$ -LiAlO<sub>2</sub> (hcp) and LiAl<sub>5</sub>O<sub>8</sub> (cubic) phases. It should be noted that some  $d$ -spacing data, which cannot be classified into either of the above two phases, are consistent with the monoclinic  $\beta$ -LiAlO<sub>2</sub> phase. It was, however, not possible to conclusively identify this phase.

*7091 Al/B<sub>4</sub>C( $\phi$ )*. The typical microstructure of the AR 7091Al/B<sub>4</sub>C composite is shown in Fig. 3(a). The average grain size of the matrix, as well as that of the B<sub>4</sub>C particles, was nominally 5  $\mu\text{m}$ , and there were several different precipitate phases dispersed along grain boundaries, in the matrix and at the interface, as seen in Fig. 3(b). Lyle and Cebulak [11], Kuo and Starke [12] and Walker and Starke [13] have identified the phase field of this alloy system. Particles of Al<sub>3</sub>(Fe,Co)<sub>2</sub> and Al<sub>7</sub>Cu<sub>2</sub>Fe were identified in the current composite by electron diffraction, and Al<sub>3</sub>(Fe,Co)<sub>2</sub> was seen to occur more frequently in the matrix.

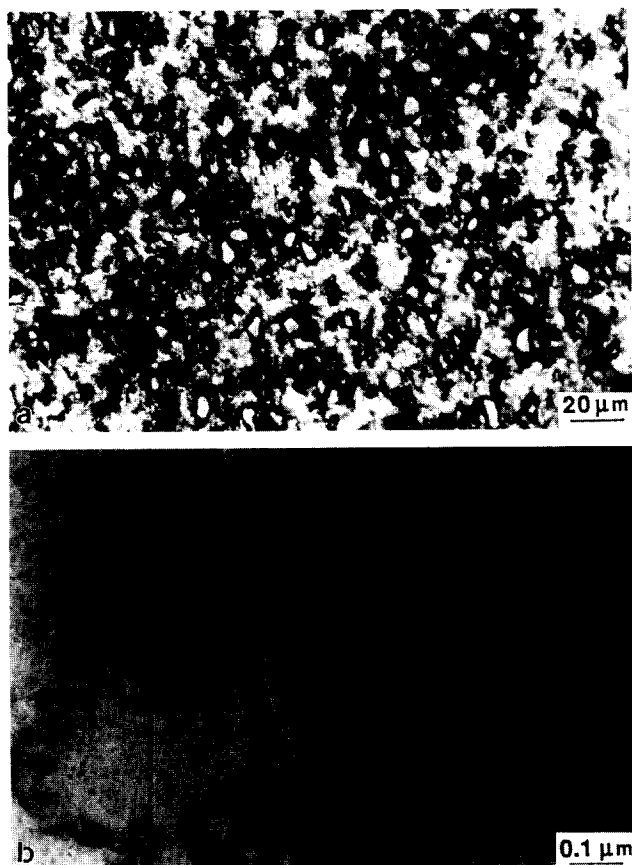


Fig. 3. (a) Optical micrograph of the polished and etched microstructure of the 7091Al/B<sub>4</sub>C composite, and (b) TEM micrograph illustrating the various precipitates dispersed in the matrix, grain boundary, and interface.

The predominant matrix precipitates included the metastable  $\eta'$  and equilibrium  $\eta$  (MgZn<sub>2</sub>) phases. The latter phase was also associated with subgrain and grain boundaries, and the largest  $\eta$  precipitates were on the order of 50 nm in size. The equilibrium  $\eta$  phase (which has a hexagonal crystal structure, with  $a = 5.21$  Å and  $c = 8.60$  Å) is known to exist with at least nine different orientation relationships with the fcc Al matrix [14]. The  $\eta_2$  type, which has a {111} habit plane, was most frequently observed. This was also confirmed in the current study. Throughout the study, no reaction products were observed along the B<sub>4</sub>C/matrix interfaces. However, some  $\eta$  precipitates were seen to be preferentially distributed along the interface and consistently wet the interface.

*Ti-6Al-4V/B<sub>4</sub>C/B<sub>0</sub>*. Figure 4 shows a SEM cross-sectional view of the Ti-6Al-4V/B<sub>4</sub>C/B as-received sample. The small inner core of the fiber is the W wire, which was used as a seed for the B and B<sub>4</sub>C deposition. Outside the original 6  $\mu$ m-thick B<sub>4</sub>C coating a TiB<sub>2</sub> continuous layer varying in thickness from 1 to 3  $\mu$ m can be seen. The outer needlelike phase has been

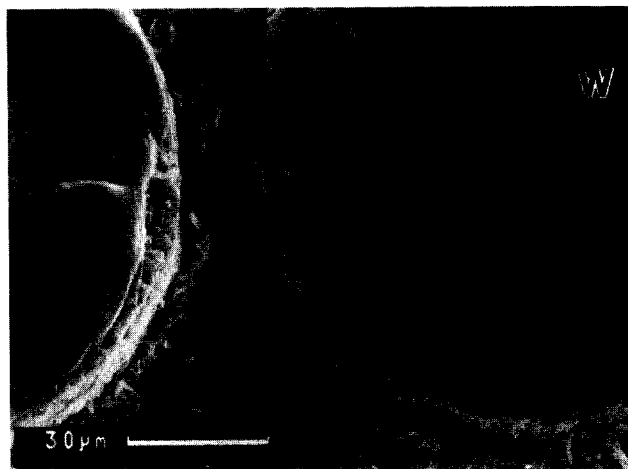


Fig. 4. SEM micrograph of the cross-sectional view of the AR Ti-6Al-4V/B<sub>4</sub>C/B composite; interfacial reaction products can clearly be seen.

identified as TiB [9]. This phase was seen to extend into the Ti matrix up to a distance of 6  $\mu$ m. It can be seen that the B<sub>4</sub>C coating did not provide sufficient protection in preventing the interdiffusion of B and Ti. This is thought to be caused by the use of prolonged heat treatments at high temperature for diffusion bonding.

### 3.1.2. General mechanical properties

Typical stress-strain curves for the Al-Li/Al<sub>2</sub>O<sub>3</sub>, 7091Al/B<sub>4</sub>C and Ti-6Al-4V/B<sub>4</sub>C/B composites in quasi-static tension and/or compression are shown in Fig. 5. For the Al-Li/Al<sub>2</sub>O<sub>3</sub> and Ti-6Al-4V/B<sub>4</sub>C/B composites, the tensile curves are seen to exhibit two distinct regions. In the initial region, the stress increases linearly with strain. Upon additional loading, the stress-strain curves deviate from linearity in stage II, which is postulated to be due to the fiber cracking normal to the applied load. The quasi-static fracture mechanism should be related to the intrinsic fiber defects (pores) in the Al-Li composite and the degraded fiber surface due to interfacial reaction in the Ti-base composite. The 7091Al/B<sub>4</sub>C composite stress-strain response also possesses three distinct regions. Observations of the fracture surface suggest that the fracture process was controlled by void formation in the matrix close to the matrix/particle interface and these voids linked by microvoid coalescence in the matrix between the B<sub>4</sub>C particles, thus leading to final failure.

The mechanical testing results for all three composites are summarized in Table 2. Calculated elastic modulus values based on the 'rule of mixture' are also included. Generally, the fiber-reinforced materials exhibited a higher strengthening effect than the particulate-reinforced composites. The Al-Li/Al<sub>2</sub>O<sub>3</sub> composite is 80% stronger than the Al-Li alloy, as opposed to the 7091Al/

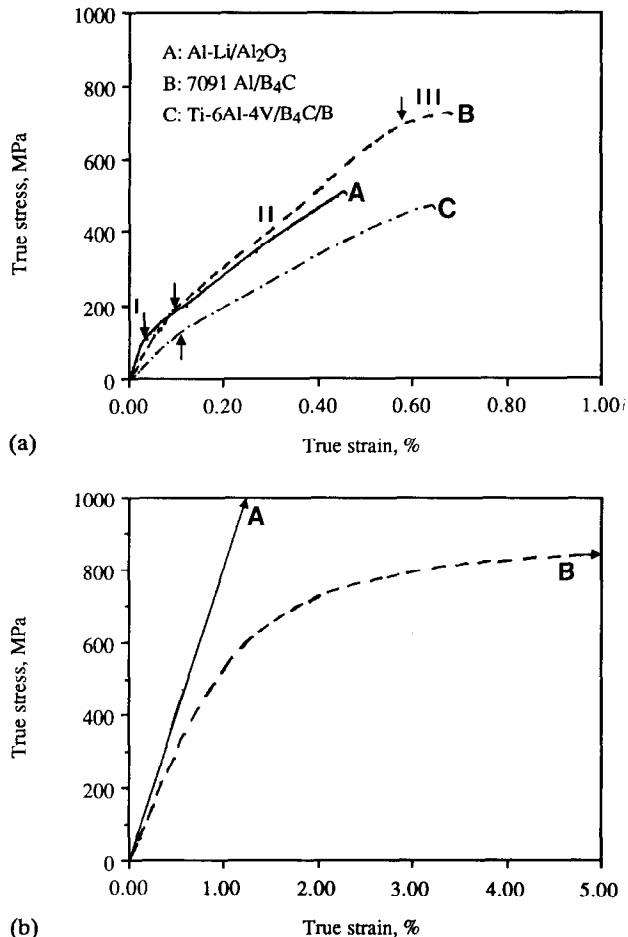


Fig. 5. Typical true stress-strain curves of the three composites tested under quasi-static conditions: (a) tension, (b) compression. The average failure stress and strain for the Al-Li and 7091 base composites under compression loading are 1500 GPa and 2.3%, and 870 GPa and 15%, respectively. The compression test on the Ti composite was not performed owing to its thin sheet nature.

$B_4C$  composite, which is only 6% stronger than unreinforced 7091 alloys. This trend is not seen in the Ti-6Al-4V/ $B_4C/B$  composite, in which case the reduction of strength appears to be due principally to the degradation of the fibers resulting from extensive interfacial reactions during over-exposed heat treatment leading to early failure near the reaction zone.

### 3.2. Effects of shock loading

#### 3.2.1. SEM and OM observations

*Al-Li/Al<sub>2</sub>O<sub>3</sub>*. Optical examination of the side view of the Al-Li/ $Al_2O_3$  samples (shock loaded with the shock wave direction parallel to the fiber direction) revealed extensive cracking of the fibers, with the resulting fiber aspect ratio ranging from 2 to 5, as seen in Fig. 6. Misalignment of the sectioned fibers is also readily apparent. Local buckling of the fibers appears to have occurred during shock loading. Cracking in the

composite appears to proceed in a path perpendicular to the fiber direction, which is not the case when shock-wave loading is applied perpendicular to the fibers (e.g., in the case of the Ti composite).

*7091Al/B<sub>4</sub>C*. Figure 7 shows cracks observed in  $B_4C$  particles in the shock-loaded 7091Al/ $B_4C$  sample. Debonding between the matrix and particles was looked for but not frequently observed in the sectioned and polished shock-loaded samples. Little apparent macroscopic damage or deformation was readily evident on the polished surface of this composite.

*Ti-6Al-4V/B<sub>4</sub>C/B*. In order to ensure that the stacking of the three composite sheets was rigid and the shock wave was transmitted with no extraordinary reflection or loss of momentum, the residual strain of these three sample sheets (in longitudinal, transverse and thickness direction) after shock loading was carefully measured. The difference in permanent residual strain was considered to be negligible; hence the three layers of sample sheets were treated (though this is not fully justifiable) as one single thick composite of 18 plies. This assumption was found to be acceptable, judging from the post-shock tensile results from the specimens sampled from these three layers. It should be noted that the three sample sheets after side-on shock loading still remained flat overall and had uniform thickness. No indication of sample bending can be traced from the post-shock measurements. Although the specimens might have the possibility of bending during shock loading, such a tendency is not expected (and is actually intended to be avoided) using the carefully designed shock assembly in this study.

Optical and SEM observations of the Ti-6Al-4V/ $B_4C/B$  composite materials revealed significant cracking of the fibers. The typical morphology of the shocked composite, seen from the cross-sectional and longitudinal directions, is shown in Fig. 8(a)-(d). Cracks were seen to propagate throughout the cross section of the composite. Crack branching was also observed (Fig. 8(c)). Fine branches are thought to correspond to crack initiation, with the branches converging into major cracks, similar to river patterns. The aspect ratio of the broken  $B_4C/B$  fibers after shock loading was about 4 to 5. Almost all of the fibers were seen to have microcracks that propagated across the fiber cross section. Some of the cracked fibers appeared to have spalled away from the surface during cutting.

#### 3.2.2. TEM observations

*Al-Li/Al<sub>2</sub>O<sub>3</sub>*. Figure 9 shows the substructure of the aluminum matrix in the Al-Li composite. A high density of tangled dislocations was observed in the matrix, especially near the fiber/matrix interface. The

TABLE 2. Summary of the quasi-static mechanical properties of the composites studied

	Al-Li-base MMC		7091-base MMC		Ti-base MMC	
	T <sup>a</sup>	C <sup>a</sup>	T	C	T	C
$\sigma_{UTS}$ (MPa)	506 ± 8	1500 ± 300	700 ± 25	874 ± 10	517 ± 24	—
$E$ (GPa)	225 (I) 97 (II)	80	220 (I) 90 (II)	60	130 (I) 68 (II)	—
$\epsilon$ (%)	111 (ave.) <sup>b</sup> 0.53 ± 0.5	2.3 ± 0.3	120 (ave.) 0.72 ± 0.5	15 ± 1	90 (ave.) 0.55 ± 0.38	—
$\sigma_{UTS-cal}$ (MPa) <sup>c</sup>	815	—	—	—	1700	—
$E_{cal}$ (GPa) <sup>c</sup>	244	—	—	—	225	—

Note: The tensile UTS,  $E$  and  $\epsilon$  properties for the base matrix alloys are: Al-Li: 280 MPa, 78 GPa and 6%; 7091 Al: 650 MPa, 72 GPa and 13%; Ti-6Al-4V: 900 MPa, 110 GPa and 13%.

<sup>a</sup>T and C refer to tensile and compressive properties; for the fiber-reinforced composites the data refer to longitudinal properties.

<sup>b</sup>Average modulus over stages I and II.

<sup>c</sup>Calculated values based on the 'rule of mixture' for the L direction.



Fig. 6. Optical micrograph of the shock-loaded Al-Li/Al<sub>2</sub>O<sub>3</sub> composite showing extensive breakage of the Al<sub>2</sub>O<sub>3</sub> fibers.

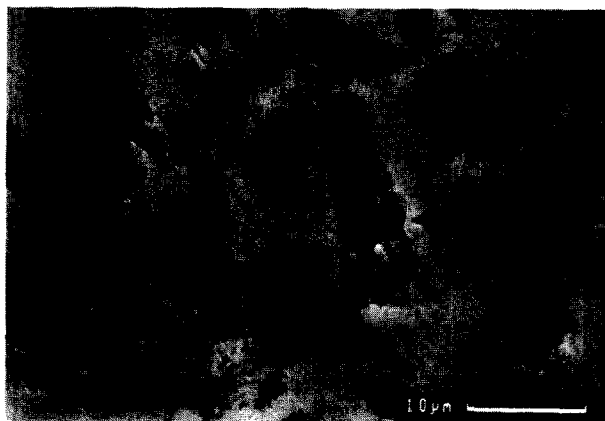


Fig. 7. SEM micrograph showing the cracking in the B<sub>4</sub>C particles in the shock-loaded 7091 Al/B<sub>4</sub>C composite.

dislocation distribution within the matrix was not uniform, its density being higher near the fibers and decreasing with increasing distance away from the fibers. A high density of tangled dislocations was typically

observed in the unreinforced metals as a result of shock-compression [4]. Since the  $\delta'$  precipitates were not formed in this composite, the dislocations did not appear to have a planar tendency, in contrast to the behavior of Al-Li base alloys, which contained  $\delta'$  precipitates [4].

*7091Al/B<sub>4</sub>C<sub>(p)</sub>*. A tangled dislocation morphology (Fig. 10(a)) similar to that seen in the Al-Li base composite was also observed in the 7091Al/B<sub>4</sub>C composite matrix. The small  $\eta'$  precipitates did not seem to produce a pronounced effect on the dislocation morphology. The substructure of the B<sub>4</sub>C particulates in the shock-loaded 7091Al/B<sub>4</sub>C samples is presented in Fig. 10(b). Deformation twins, lying on {0001} and/or {1120} planes, were seen within the B<sub>4</sub>C (hcp) particles exposed to shock-wave prestraining.

*Ti-6Al-4V/B<sub>4</sub>C/B<sub>(p)</sub>*. Owing to the debonding and splitting of the fibers as a result of shock loading, the fibers in this composite were absent after ion milling. The deformed microstructure of the reaction zone and the matrix near the fiber/matrix interface was thus not characterized. What could be seen were the shock-loaded  $\alpha$  and  $\beta$  matrix grains. No evidence of shock-induced phase transition products, such as the omega phase, were seen in the Ti-6Al-4V matrix following shock prestraining. The most noticeable features observed in the matrix grains were planar slip lines, sometimes forming well-defined bands. Single and multiple slip-line variants were seen in different grains, lying on {0001} and {2110} planes in the  $\alpha$ -grains and {112} in the  $\beta$ -phase grains. Figure 11(a) shows the morphology of two crossing slip bands on two {112} planes, seen in a  $\langle 110 \rangle$  zone axis. Between the slip bands, the dislocation density was fairly low, as compared with the matrix in the two other composites. It appears

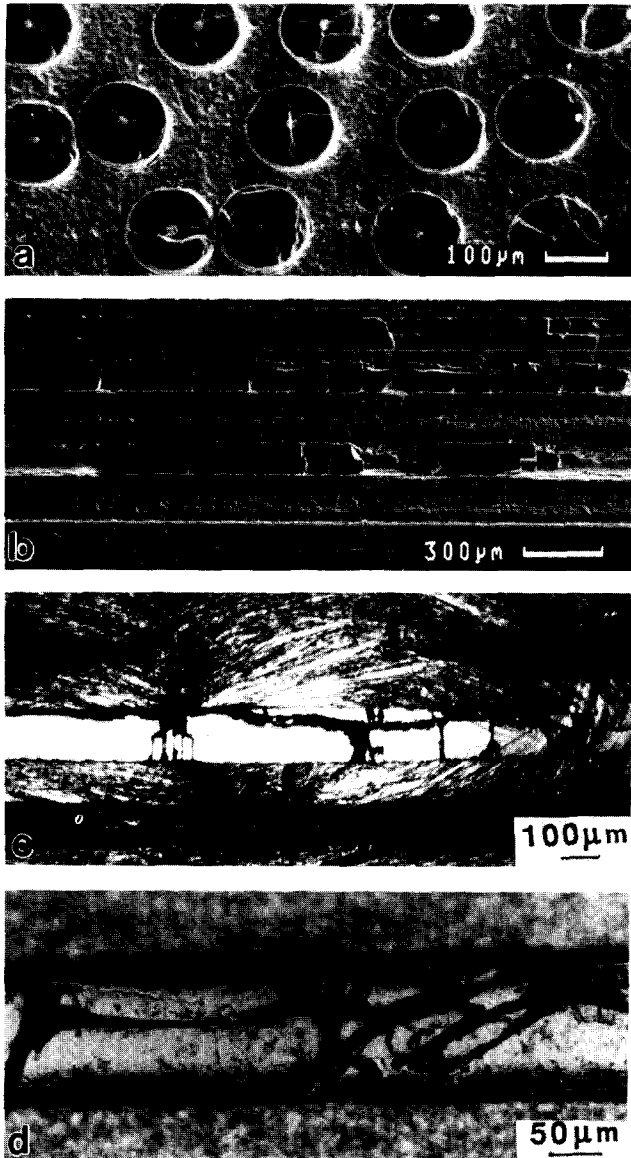


Fig. 8. Optical or SEM micrographs of the cross-sectional (a) and longitudinal (b)–(d) views of the shock-loaded Ti-6Al-4V/ $B_4C/B$  composite. Multiple cracking modes can be seen in (b)–(d). The incident shock wave direction is from top to bottom in these figures.

that the Ti matrix deformed in a more planar manner than the aluminum composites. Another interesting substructure in the shock-loaded Ti-6Al-4V matrix was deformation twins in both the  $\alpha$  (predominantly on  $\{11\bar{2}1\}$ ) and  $\beta$  (solely on  $\{112\}$ ) grains. The volume fraction of both types of twins was very low, probably because of the low peak shock pressure in this study. Based on diffraction pattern analysis, these twins were determined to be compound-type twins in the bcc  $\beta$  grains lying on  $\{112\}$  planes (Fig. 11(b)), which is similar to the twin orientation found in shock-loaded high-purity Nb [15].

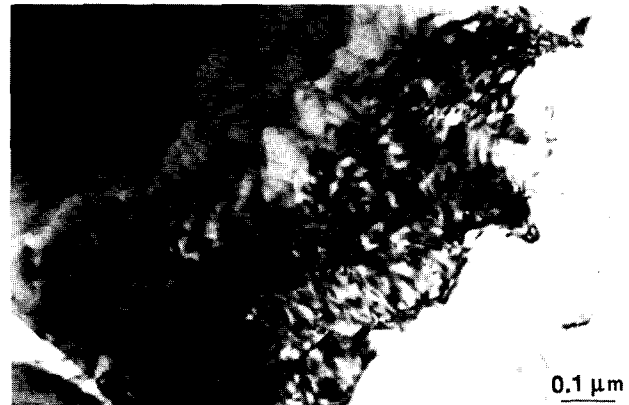


Fig. 9. TEM micrograph of the shock-loaded Al-Li/ $Al_2O_3$  composite, showing a high density of tangled dislocations in the matrix.

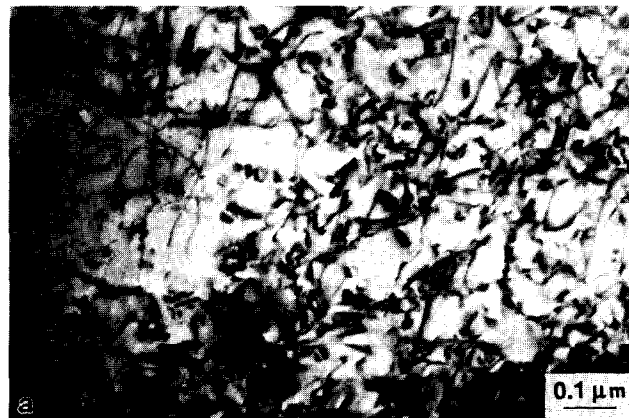


Fig. 10. TEM micrograph illustrating (a) tangled dislocations in the matrix and (b) deformation twins. The twins have been seen on  $\{0001\}$  and/or  $\{11\bar{2}0\}$  planes within the  $B_4C$  particles in the shock-loaded 7091 Al/ $B_4C$  composite.

### 3.3. Quasi-static tension or compression loading of as-received and shock-prestrained samples

3.3.1. Comparison of composite mechanical response  
 Al-Li/ $Al_2O_3$ . The true stress-strain curves from a quasi-static compression test on the AR and SP Al-Li/ $Al_2O_3$  composites are given in Fig. 12(a). The typical

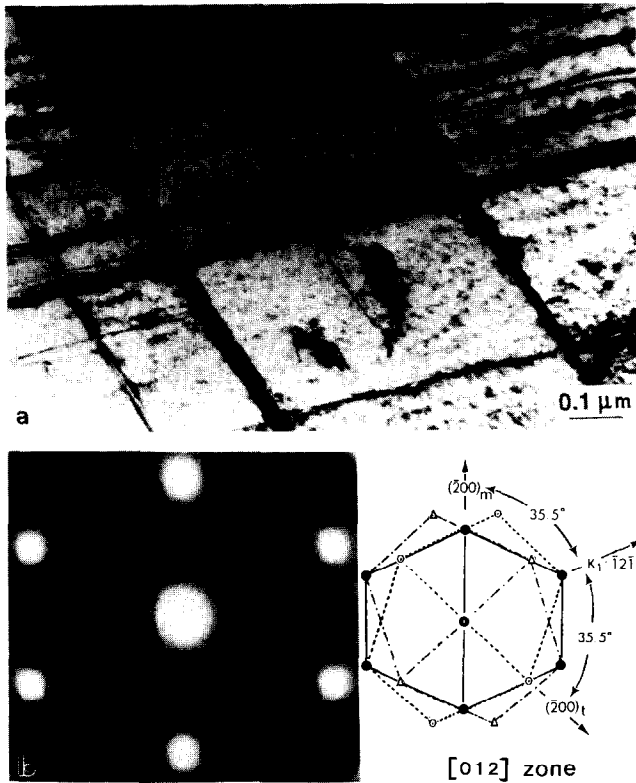
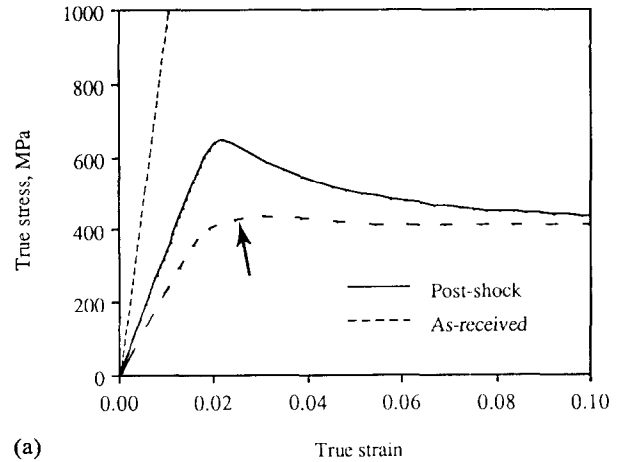


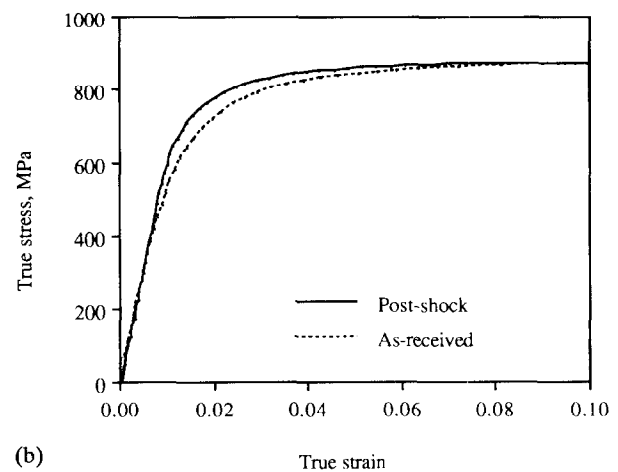
Fig. 11. (a) TEM micrograph showing two variants of planar slip bands, and (b) TEM diffraction pattern with weak twin reflections, both in  $\beta$  grains of the shock-loaded Ti-6Al-4V/B<sub>4</sub>C/B composite.

compression response of the AR composite exhibited a relatively high yield strength ( $> 1200$  MPa) and elastic modulus ( $\approx 80$  GPa), accompanied by a low plastic strain to failure ( $\approx 2.5\%$ ). However, in one instance the tiny compression specimen was not exactly aligned during loading and the composite deformed by shear and buckling, resulting in a greatly reduced yield strength ( $\approx 450$  MPa), low modulus ( $\approx 25$  GPa) and a greatly increased total failure elongation (30%), as seen from the lower AR curve in Fig. 12(a).

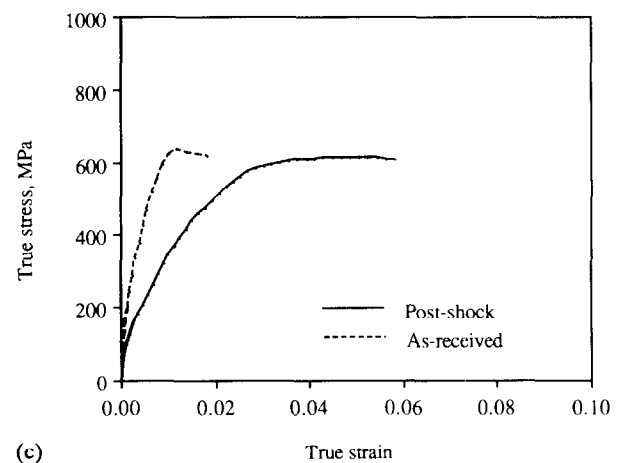
As shown in Fig. 6, the primary mode of deformation of this composite subjected to shock loading along its fiber direction was failure of the Al<sub>2</sub>O<sub>3</sub> continuous fibers. In the SP reload compression tests the fractured but still somewhat intact portions of the fibers were seen to sustain a load up to  $\approx 600$  MPa initially, with a reduced elastic modulus of 35 GPa. In this case, the mechanical response was more like an aligned short-fiber composite. However, after slight straining the cracking fibers collapsed and the stress dropped rapidly. At plastic strains exceeding 2% the collapsed fiber sections could not support further loading. The deformation mode in the SP sample then shifted to shearing in the matrix, approaching the curve of the AR tiny sample in 'shear' mode. The average failure strain of



(a)



(b)



(c)

Fig. 12. True stress-strain curves of the post-shock reload tests for the three composites: (a) Al-Li/Al<sub>2</sub>O<sub>3</sub> under compression; (b) 7091Al/B<sub>4</sub>C under compression; (c) Ti-6Al-4V/B<sub>4</sub>C/B under tension. The lower AR curve in (a), indicated with an arrow, was obtained when the compression sample was not properly aligned during loading.

the SP samples was found to be 18%. From the above results, it appears that the SP reload sample was degraded during the shock prestraining, in terms of a marked reduction in strength and modulus and a sub-

stantial increase in failure strain, as compared to the properly aligned compression AR composites.

*7091Al/B<sub>4</sub>C<sub>(p)</sub>*. Representative stress–strain curves obtained from compression tests on the AR and SP 7091Al/B<sub>4</sub>C composites are shown in Fig. 12(b). The maximum compressive flow stress of both specimens reached  $\approx 870$  MPa at 10% strain, and this strength was maintained until failure (14–18%). The strength of the AR and SP particulate-reinforced specimens did not appear to be appreciably different. This was also true for the elastic modulus – both were  $\approx 60$  GPa for the tiny compressive samples. Shock loading was not seen to cause any significant effect on the mechanical properties of the 7091Al/B<sub>4</sub>C composite, and it is postulated that this is related to the fact that the damage induced in the B<sub>4</sub>C particles and at the matrix/particle interfaces by shock-prestraining was not sufficient to significantly alter the flow stress. However, dislocation generation and storage in the 7091Al matrix during shock loading yielded a slight increase in the reload yield strength of the composite. If the reload test had been conducted in tension, a certain degree of strength degradation might have been expected.

*Ti-6Al-4V/B<sub>4</sub>C/B<sub>0</sub>*. Figure 12(c) demonstrates the typical tension (not compression) response of the Ti-6Al-4V/B<sub>4</sub>C/B composite materials. In order to ensure that the effect from stacking three composite sheets may be minor, post-shock tensile tests were conducted on three specimens sampled from each sheet, and the results supported the original assumption. The tensile loading axis here was parallel to the fiber direction, i.e., a 90° loading axis change from the shock-loading axis. The strength of the SP reload composites appeared to be only slightly lower than that of the AR composite. Strengthening from shock prestraining in the Ti matrix appears to have been balanced by weakening of the composite due to fiber cracking and interface splitting. In contrast, the elastic modulus of the shocked composite dropped significantly, compared with that of the AR material. The former was only one third of the latter (owing to the nonlinearity from the beginning of the stress–strain curves, only the average elastic modulus for the first 1% strain can be extracted, and the values are  $100 \pm 4$  and  $35 \pm 3$  GPa for the AR and SP specimens). On the other hand, the total failure strain of the shock-loaded composite increased from 2% for the AR composite to nearly 6% (note that 6% strain for a fiber-reinforced composite under tension is exceptional). The increase in the fracture strain and loss of stiffness in the composite are considered to be due to damage to the fibers themselves and to the fiber/matrix interface bond strength. In fact, since the fibers have become fragmental, the SP Ti composite may be

viewed as reinforced by discontinuous fibers. The higher elongation and lower modulus in the SP sample may simply be the result of transformation from continuous to discontinuous fibers.

### 3.3.2. SEM observations of composites

The SEM surface characterization detailed below involved both the post-shock reload tests on the tension samples, and the quasi-static tension/compression tests on the as-received composites. It should be noted that there are no post-shock reload tension tests for the small Al-Li/Al<sub>2</sub>O<sub>3</sub> and 7091Al/B<sub>4</sub>C composites, since the shock-loaded samples themselves were too small to allow tensile specimens to be machined from the post-shock composites.

*Al-Li/Al<sub>2</sub>O<sub>3(p)</sub>*. It is more difficult to test fiber-reinforced composites under compression, owing to buckling, brooming, and axial misalignment problems. The failure mode in both the SP and AR small Al-Li/Al<sub>2</sub>O<sub>3</sub> composites, as well as in the larger compressive samples, under quasi-static compression loading was seen to be mainly by kinking and brooming. Similar observations were reported by Shetty and Chou [16]. As seen from the longitudinal section of the kinked AR Al-Li/Al<sub>2</sub>O<sub>3</sub> specimen (Fig. 13(a)), failure tended to initiate from the bottom of the specimen (typical brooming).

Following quasi-static tensile deformation, the AR Al-Li/Al<sub>2</sub>O<sub>3</sub> composites (larger samples) exhibited a highly ductile matrix. Figure 13(b) shows evidence of fiber pullout and interface failure. Examination of the fracture surface at a higher magnification showed failure at the fiber matrix interface and also the formation of voids at the interface. The resultant tensile fracture surface of the AR Al-Li/Al<sub>2</sub>O<sub>3</sub> composites is, however, macroscopically planar, compared with the fracture surfaces of the AR Ti composites and the AR Al-Li/Al<sub>2</sub>O<sub>3</sub> composites under Charpy impact fracture.

*7091Al/B<sub>4</sub>C<sub>(p)</sub>*. Only a minimal amount of information could be extracted from the SP and AR ‘tiny’ compressive samples loaded to  $\approx 10\%$  strain. Both of the samples remained intact, consistent with the maintenance of high strength of these particulate-reinforced composites. Shock loading did not appear to cause any appreciable effect on the mechanical response of this material as probed in compression.

The fracture surface of the large AR tensile sample was observed to contain fractured or decohered B<sub>4</sub>C particles, as indicated in Fig. 14. The wetting between the matrix and the B<sub>4</sub>C particles appeared to be good, suggesting a moderately strong cohesion between the matrix and particles. This observation is supported by the high ratio of cracked to decohered particles seen in the fracture surface of the tensile specimens. The

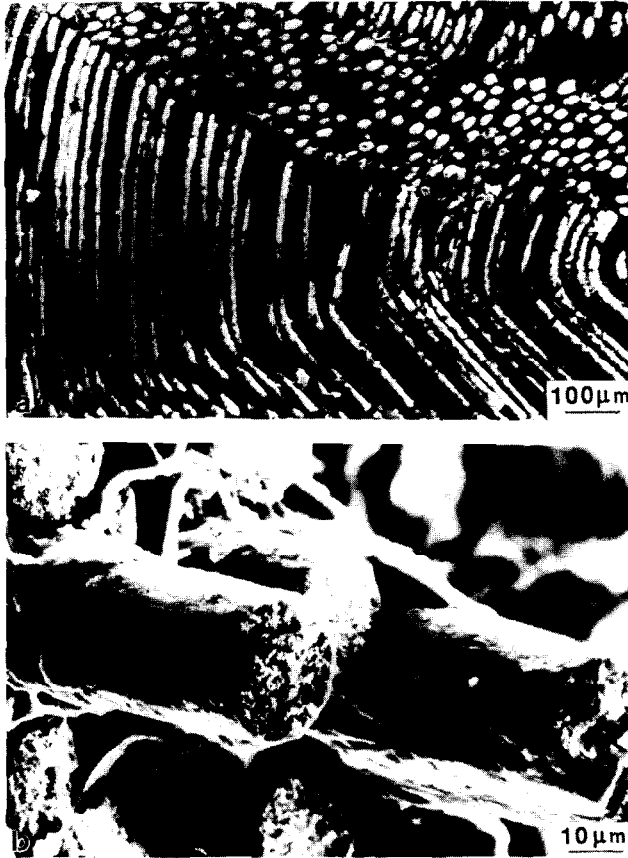


Fig. 13. (a) Optical micrograph showing the kinking effect; (b) SEM micrograph showing fiber pullout and interface failure in the AR Al-Li/Al<sub>2</sub>O<sub>3</sub> composite tested at a low rate.

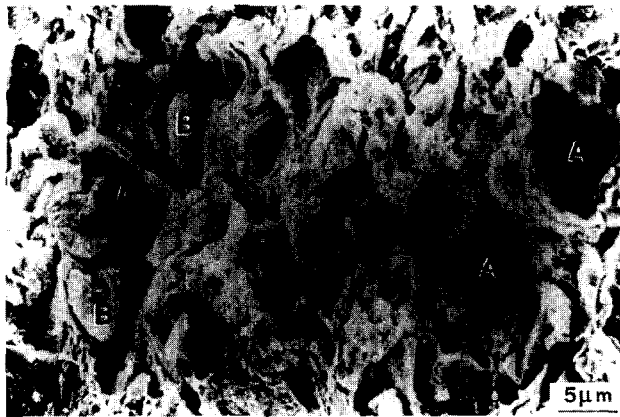


Fig. 14. SEM micrograph of the AR 7091Al/B<sub>4</sub>C composite tested under tension, showing broken B<sub>4</sub>C particles (indicated by A) and particle decohesion (indicated by B). A certain degree of plastic deformation in the 7091 Al matrix can also be seen.

cracks in the broken particles occurred perpendicular to the tensile axis and opened with deformation; this will induce a strain concentration in their vicinity. Detailed analysis showed that the cracked particles outnumbered the decohered particles by a ratio of almost 2:1. This ratio gives some indication of the local

bonding strength of the B<sub>4</sub>C/matrix interface. There is also evidence of void formation and void growth around the B<sub>4</sub>C/matrix interface. Most of the B<sub>4</sub>C particles exhibited single-faced transverse fracture on the fracture surface, which was in distinct contrast with the multiple cracking in the shock-loaded 7091/B<sub>4</sub>C samples (Fig. 7).

*Ti-6Al-4V/B<sub>4</sub>C/B<sub>6</sub>*. The topographic side-view of the fracture surface in the SP tensile reload 'tiny' Ti-6Al-4V/B<sub>4</sub>C/B sample revealed a significant amount of fiber pullout and matrix plastic deformation. This is in contrast to the much flatter fracture surface in the AR composite. It is obvious that the fibers failed from cracks which were induced by the side-on shock impact. This is seen from the irregular stepped fracture surface of the fiber in the SP sample, instead of the relatively flatter surface typical for brittle failure in the AR composite. Examples are shown in Fig. 15(a) and (d). Though there is still a certain level of pullout in the as-received composite (Fig. 15(d)), the occurrence frequency and extent were comparably less significant. This result is consistent with the tensile loading where the elongation of the shocked composite exhibited a much higher value. It should be noted that the extensive interfacial reaction in the AR Ti composite involves volume change and thus residual stress along the interface. This will promote fiber cracking even without shock prestraining, leading to a certain level of fiber debonding and pullout, as well as the lower elastic modulus than the ROM value, in the as-received composite. The above statements regarding the extent of fiber pullout and the resulting tensile elongation and modulus in the AR and SP Ti composites are made in a relative sense.

It can be seen that the majority of the fibers, whether SP or AR composite, were separated from the matrix at the interface between the B<sub>4</sub>C and reaction products (Fig. 15(b)) rather than from the reaction products and the Ti matrix. The brittle and chapped TiB<sub>2</sub> layer can be seen to debond from the fibers. A similar situation has been found in other Ti-base composites under quasi-static loading where the fracture path was close to the fiber side of the reaction zone [17]. In addition, splitting between the B and B<sub>4</sub>C coating layer was also observed occasionally in the SP (but not in the AR) specimen; one example is shown in Fig. 15(c). Based on these observations, it is postulated that the reaction products do not form a strong bond with the B<sub>4</sub>C coating layer, leading to interface splitting and further fiber pullout from this interface, especially for the SP specimens. Conversely, the outer needle-shaped TiB phase grows into the Ti matrix, resulting in relatively stronger bonding compared with the bond between the B<sub>4</sub>C/TiB<sub>2</sub>.

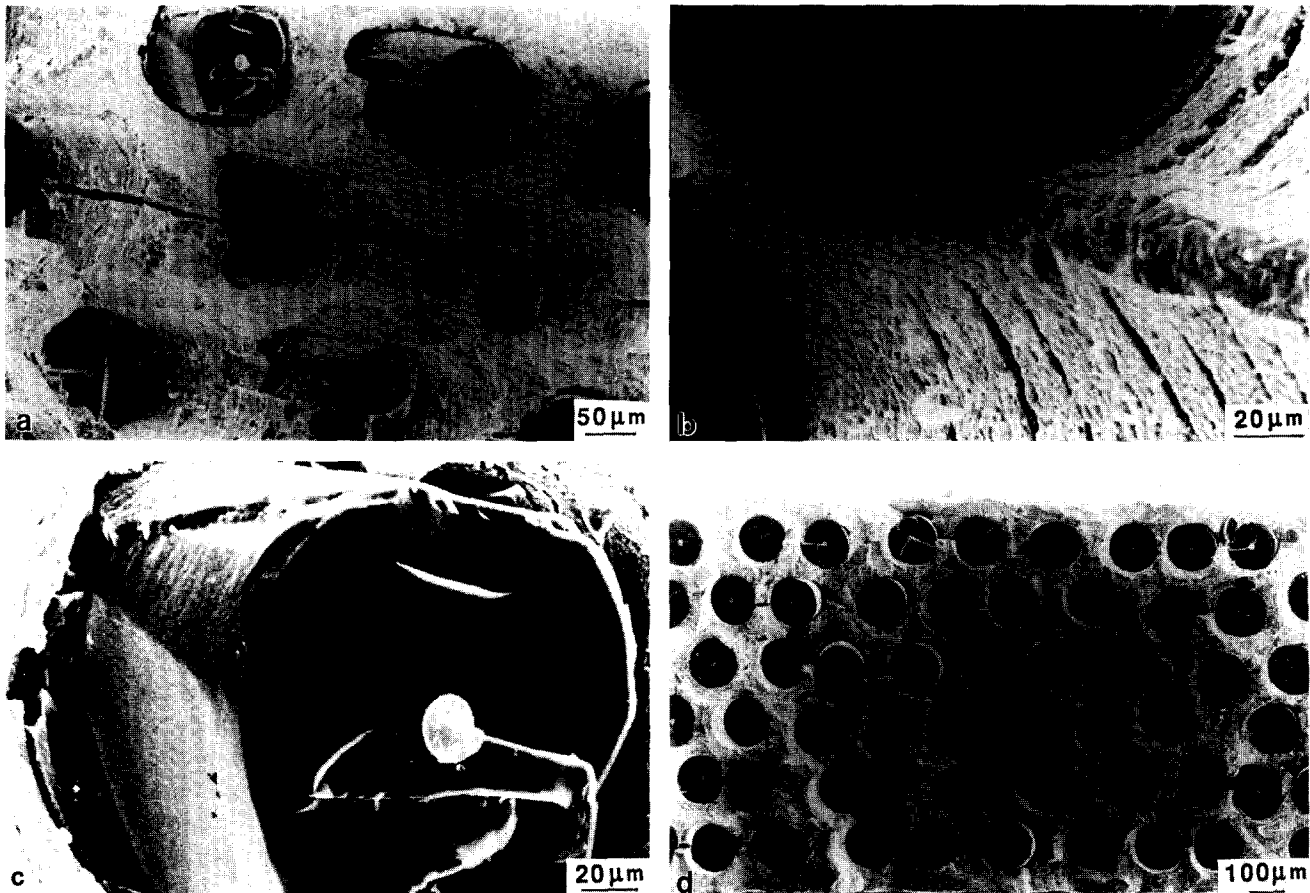


Fig. 15. SEM micrographs of the fracture surfaces: (a)–(c) post-shock reload, and (d) as-received Ti-6Al-4V/B<sub>4</sub>C/B composites. The fibers were most often seen to separate from the matrix at the interface between the B<sub>4</sub>C coating and reaction products in both the SP and AR samples, as shown in (b). But in SP sample interface splitting between the B and B<sub>4</sub>C coating layer has also been observed occasionally, as seen in (c). The fracture surface of the AR sample (d) was seen to be much more planar and brittle.

## 4. Discussion

### 4.1. Effects of loading rate on MMC response

The influence of loading (or strain) rate on a variety of metals and alloys has been well characterized (e.g., [2–5]). Most materials, when the adiabatic heating effect is not pronounced, show increased flow stress levels at high rates, i.e., an apparent positive strain rate sensitivity. The major cause of this strengthening is thought to be increased dislocation generation and storage at high rates. No extensive damage accumulation processes in terms of, for example, microcracks or decohesion along grain boundaries, are observed in most metal systems. This is not the case for the MMC materials. For the fiber-reinforced materials, the fiber/matrix interface is probably the most critical region in a MMC, since the mechanical properties are largely limited by the efficiency of the fiber/matrix bond.

From a macro-scaled viewpoint, particularly as regards the matrix, shock loading did not significantly alter the composites to any large extent. On the other hand, from a micro-scaled viewpoint, the shock was observed

to cause local damage to the reinforcements (fibers or particulates) within the MMCs. The difficulty with 1-D shock waves, from an engineering point of view, is that the residual strain after loading is small, i.e., minimal dimensional change can be traced from a macroscopic viewpoint if the shock-loading experimental design minimized late-time lateral loading effects. In this regard, the composite appears unaltered macroscopically. In reality, however, the internal properties and integrity of the composite may have been severely altered, as seen in this study by the propensity of reinforcement breakage, debonding, and local deformation in the matrix and reinforcement.

It is meaningful to explore the microstructure evolution in a matrix reinforced by different types of reinforcements under impact or shock-wave loading and relate these observations to what is known about the shock response of alloys containing small precipitates, dispersoids and/or inclusions. In the case of particulate-reinforced composites, the compressive shock wave, as well as the release wave, propagate through a heterogeneous mixture comprised of the metal matrix and

ceramic particulates. Owing to the drastically different elastic and plastic behavior of each constituent, each phase experiences a different local response to the propagating shock wave, which in turn is averaged to produce a bulk response. The large disparity in elastic sound speed between the ceramic reinforcements (the data on  $V_s$  for the Al, Ti and ceramic reinforcements are  $\approx 5.8$ ,  $5.3$  and  $10.0 \text{ km s}^{-1}$ ), which possess high sound speeds, and the metal matrix alloys will in addition produce local dispersion of the propagating shock pulse. Owing to this local dispersion and structural and mechanical anisotropy, quantitative prediction of the local stress state is difficult at best. Extensive systematic research is required to resolve the shock mechanics applicable to composite behavior. In addition to the first-order loading uncertainties, the global uniaxial strain conditions within a 1-D shock may actually result in locally resolved tensile loading on reinforcement segments owing to inadequate matrix accommodation of the applied stresses. In addition to the issues related to non-uniform application of the compressive pulse, it is release waves, which are formed because of internal impedance mismatching and interface phenomena, that will certainly cause widespread damage to the composite.

Interaction of release waves within a composite can further lead to locally high tensile loading within the composite. Wave propagation from these multiple reflections may, however, be offset within a bulk composite, possessing high constraint by reinforcing particles, by the plastic response of the matrix. The continuous matrix, which is highly 'plastic' compared to the ceramic reinforcement, plays an important role in absorbing and accommodating the passing high-energy wave via plastic deformation. Observations in the current study suggest that the deformation modes in the metal matrices in particulate-reinforced composites appear to resemble those seen in the conventional unreinforced metals in many ways. In the particulate-reinforced composite the impact loading may also produce deformation in the reinforcement such as dislocations, twins or microcracks, as seen in the  $\text{B}_4\text{C}$  particles. In a few instances, local debonding was also found, but its occurrence was too low to result in large effects on the bulk deformation response. In short, it is thought that low amplitude ( $< 10 \text{ GPa}$ ) 1-D shock loading acting on a particulate-reinforced composite will not yield severe overall damage. The composite will still maintain many of its bulk properties after shock loading, consistent with the experimental results. However, a certain level of degradation is expected when the reload is carried out under tension.

The shock wave loading response of long-fiber-reinforced composites was conversely seen to be much more severe, although the volume fractions of the continuously reinforced composites, both the aluminum and titanium

matrix composites, were both higher than the particulate Al-matrix case. Independent of whether the shock-wave direction was parallel (as in the case of Al-Li/ $\text{Al}_2\text{O}_3$ ) or perpendicular (Ti-6Al-4V/ $\text{B}_4\text{C}/\text{B}$ ) to the continuous fibers, the fibers were fragmented into numerous pieces in response to the sudden high-energy loading pulse. Given the uniformly small residual strains in the shock-recovered composites, the major portion of the locally observed fracture response appears to be attributable to the significant influence of constraint on composite response in the fiber-reinforced composites. Several breakage mechanisms are briefly postulated below.

As the shock wave traveled parallel to the fibers, the strains experienced by the  $\text{Al}_2\text{O}_3$  fibers must have exceeded the elastic regime, based on the metallographic observations. Since the dynamically deformed region at the wave front is only a very localized volume, constraint from the surrounding matrix regions will prevent the fiber section within the localized volume from extensive kinking (either in phase or out of phase with respect to each other). Owing to this constraint the most likely relaxation mechanism, except for twinning as in the Ti-composite case, is failure. In the  $\text{Al}_2\text{O}_3$ -fiber case most of the cracks were observed to be perpendicular to the fiber axis. No crack branching or cracking along the  $45^\circ$  plane is expected. The wave velocity of the shock within the ceramic fiber and the metal matrix will not be the same. This was first thought to perhaps be a driving force in separating the fibers and the matrix; however, this was not seen experimentally. It may be due to the small partial vector of the applied stress perpendicular to the fiber; most of the force was acting along the fiber axis. The periodic breakage of the fibers may also reflect the impingement of reflected wave interactions, leading to off-axis fiber loading and cracking. Overall, this cracking did reduce the tendency for interface debonding or splitting.

When the shock wave loading was applied perpendicular to the fibers, the long fibers were observed to fail readily. Cracking within the fibers was found to be diverse, some of them having several branching cracks (see Fig. 8). The fine branches also indicate the site of crack initiation, which was usually at the bottom of the fiber (the side away from the incident shock wave, under tensile stress). It has been thought that the fiber breakage might have been resulted from the macroscopic sample bending. However, no evidence of any residual bulk bending was observed for this side-on shock loading. Nevertheless, it is believed that local bending stresses did occur during impact, owing to local material and thus stress distribution heterogeneity. Such local bending stresses will initiate the branching cracks. Once the fibers undergo branching cracking, the tendency for buck bending will be largely reduced. Meanwhile, the release wave may also play a significant role

in splitting the fiber/matrix interface, since the force vector is now perpendicular to the fiber and the interface. Severe debonding and thus fiber pullout in the post-shock tension tests were frequently observed. The release wave also appeared to have acted on the interface between the diffusion-bonded plies of the Ti-base composite, since some delaminations were seen in this study (e.g., Fig. 15).

The above comparison on the geometric effects of shock loading was made without considering material dependence. Because of the different extent of interfacial reaction in the Al and Ti composites, the tendency for interface splitting and pullout should be material dependent. Nevertheless, the basic picture for the propagation of a compressive shock wave and the reflection into a tensile wave will be similar in most ceramic-reinforced metal matrix composites. Overall it is seen from this study that fiber-reinforced MMCs can be markedly degraded by a reduction in both their strength and modulus. The latter is observed to be more severe, with the modulus of the SP composites being one third to one half that of the AR specimens. An apparent increase in the failure strain was also seen, but this will be of no significant benefit for engineering applications. Furthermore, the current results can be strengthened by the experiments using tensile tests on the SP Al-Li/Al<sub>2</sub>O<sub>3</sub> and 7091Al/B<sub>4</sub>C composites. In order to draw a more generalized picture of the shock response, studies along this line are worthwhile.

#### 4.2. Comparison between the shock effects in MMCs and their base matrix alloys

Shock-loading experiments have been conducted on a variety of aluminum base alloys, such as 6061 [18], Al-Mg [19] and Al-Li [4] systems. These results confirmed that tangled dislocations are observed following low-pressure shocks (<5 GPa), and slip bands (and/or twins) may also be seen at higher pressures (>10 GPa). The presence of ordered precipitates in Al-Li base alloys usually promotes a tendency for planar slip, thereby promoting localized deformation over the whole range of shock pressures. The matrix materials in the current composites were Al-Li and 7091Al alloys. The observation of a high density of tangled dislocations is consistent with the findings in most aluminum base alloys without ordered precipitates, which was the case in the current aluminum matrix, bearing in mind that there were no ordered  $\delta'$  precipitates formed in the Al-Li matrix. Although to the best of the authors' knowledge, shock deformation in 7091 Al has not been characterized, it is expected to exhibit substructures similar to that seen in the 6061-T6 aluminum. The random dislocation microstructure in the 7091-base matrix resembles that seen in 6061-T6 shocked to a comparable pressure. In other words, there is no evi-

dence suggesting any significant influence of shock-wave deformation on the 7091 matrix, owing principally to the presence of reinforcement constraint in the current MMCs.

The substructure in a previously studied Ti-6Al-4V alloy shock-loaded at 5, 10 and 13 GPa [20] exhibited mainly planar slip bands and twins similar to the Ti-matrix composite. The twin character appears to be similar in the alloy and the composite, which again suggests a similar deformation response in both cases. Shock strengthening in the monolithic Ti-6Al-4V alloy was found to be positive but not significant [20]. Significant strengthening of the current Ti-base composite due to the shock prestrain is thought to have been offset by the fiber degradation noted. The increase in dislocation or band/twin density in all the base matrices of the MMCs due to shock prestraining did not raise the composite strengths to any appreciable extent. This is postulated to be partly because of the low work hardening nature of Al and Ti alloy materials, and partly because of the primary strength control by the reinforcement and interface in composites. In this case any small strengthening effect due to shock prestraining on dislocation storage in the matrix can easily be overshadowed by reinforcement failure or interface debonding.

## Conclusions

The mechanical response and substructure evolution of Al-Li/Al<sub>2</sub>O<sub>3</sub>(<sub>f</sub>), 7091Al/B<sub>4</sub>C(<sub>p</sub>) and Ti-6Al-4V/B<sub>4</sub>C/B(<sub>f</sub>) composites under shock and quasi-static loading have been examined. Emphasis was placed on the influence of loading rate and loading direction, as well as reinforcement type, on the microstructural and mechanical response of several commercial MMCs. The interfacial reaction products in  $\alpha$ -LiAlO<sub>2</sub> and LiAl<sub>5</sub>O<sub>8</sub> in the Al-Li base composites, as well as the continuous-layer TiB<sub>2</sub> and needle-shaped TiB phases in the Ti-base composite, were confirmed, consistent with previous studies. In the 7091 composite, no apparent interfacial reaction phase was observed, only some  $\eta$  precipitates preferentially distributed along the interface. Interfacial bonding between the matrix and fiber reinforcement appears to be stronger in the Al-Li composite than in the Ti-base composite in the current study, judging from the debonding and pullout behavior in the as-received quasi-statically deformed materials. The weakest interface was found to be that between the matrix/reaction zone in the Al-Li composite and the fiber coating/reaction zone in the Ti-base composite. The wetting between the 7091 matrix and the B<sub>4</sub>C particles was seen to be satisfactory, while the bonding strength was only mediocre.

Shock loading on the composites resulted in various degrees of damage and plastic deformation. For fiber-reinforced MMCs, independent of whether the shock-loading axis was parallel or perpendicular to the fiber orientation, severe fiber breakage was observed. The degradation in the fibers resulted in an apparent increase in the failure strain and a considerable loss in the elastic modulus. Bonding failure was particularly prevalent in the Ti-base composite where shock wave deformation loaded the material from its transverse direction. Debonding and fiber pullout were evident in the quasi-statically reloaded shock-prestrained Ti composite. Release wave interactions are thought to be a major cause of fiber and interface damage. For the particulate-reinforced composite, shock-induced damage was not as pronounced. Only local cracking or a few instances of debonding were observed in the particulate-reinforced composite. These observations are consistent with the results of reload tests, where almost identical stress-strain curves were obtained for the as-received and shock-loaded 7091 particulate composite specimens.

The sudden passage of a high-rate stress wave or shock wave through composite materials may induce a number of permanent mechanical changes. Based on the insight gained from shock-recovered metals, shock loading on Ti- or Al-base alloys to  $\approx 5$  GPa peak pressure levels does not appreciably alter the post-shock mechanical response. In fact, a certain level of strengthening was typically observed. However, owing to the brittle nature of reinforcing fibers or particulates in composites, they will be highly susceptible to interior shock damage due to anisotropic elastic and plastic loading effects, which in turn lead to significant changes in their post-shock mechanical response.

#### Acknowledgements

The authors wish to express their gratitude to Professor J.-M. Yang at UCLA for providing the material used in this study. This research was supported by the National Science Council of Taiwan, ROC, and partly

supported under the auspices of the US Department of Energy.

#### References

- 1 C. M. Friend, *Mater. Sci. Technol.*, **5** (1989) 1.
- 2 L. E. Murr, in M. A. Meyers and L. E. Murr (eds.), *Shock Wave and High-Strain-Rate Phenomena in Metals: Concepts and Applications*, Plenum, New York, 1981.
- 3 J. C. Huang and G. T. Gray III, *Acta Metall.*, **37** (1989) 3335.
- 4 J. C. Huang and G. T. Gray III, *Metall. Trans. A*, **20** (1989) 1061.
- 5 L. B. Greszczuk, in J. A. Zukas (ed.), *Impact Dynamics*, Wiley, New York, 1982.
- 6 P. S. DeCarli and M. A. Meyers, in M. A. Meyers and L. E. Murr (eds.), *Shock Wave and High-Strain-Rate Phenomena in Metals: Concepts and Applications*, Plenum, New York, 1981, p. 341.
- 7 J. A. Cornie, Y.-M. Chiang, D. R. Uhlmann, A. Mortensen and J. M. Collins, *Am. Ceram. Soc. Bull.*, **65** (1986) 293.
- 8 A. K. Dhingra, *Philos. Trans. R. Soc. London, Ser. A*, **294** (1980) 411.
- 9 A. G. Metcalfe, in A. G. Metcalfe (ed.), *Composite Materials, Vol. I, Interfaces in Metal Matrix Composites*, Academic Press, New York, 1974, p. 113.
- 10 A. P. Majidi and T. W. Chou, *Proc. 6th Int. Conf. Composite Materials and 2nd Eur. Conf. Composite Materials, 1987*, Vol. 2, p. 422.
- 11 J. P. Lyle and W. S. Cebulak, *Metall. Trans. A*, **6** (1975) 685.
- 12 W. C. Kuo and E. A. Starke, Jr., *Metall. Trans. A*, **14** (1983) 435.
- 13 J. A. Walker and E. A. Starke, Jr., *Powder Metall.*, **26** (1983) 185.
- 14 J. Gjønnnes and C. J. Simensen, *Acta Metall.*, **18** (1970) 881.
- 15 J. C. Huang and G. T. Gray III, *Mater. Sci. Eng. A*, **103** (1988) 241.
- 16 H. R. Shetty and T. W. Chou, *Metall. Trans. A*, **16** (1985) 853.
- 17 D. S. Mahuliker, Y. H. Park and H. L. Marcus, in G. C. Sih and P. S. Theocaris (eds.), *Proc. 1st USA-Greece Symp. on Mixed Mode Crack Propagation*, Sijthoff & Noordhoff, Rockville, MD, 1981, p. 385.
- 18 G. T. Gray III and P. S. Follansbee, in S. C. Schmidt and N. C. Holmes (eds.), *Shock Waves in Condensed Matter*, Elsevier, Amsterdam, 1988, p. 339.
- 19 G. T. Gray III, *Acta Metall.*, **36** (1988) 1745.
- 20 G. T. Gray III and C. E. Morris, in P. Lacombe, R. Tricot and G. Beranger (eds.), *Proc. 6th World Conf. Titanium*, Les Editions de Physique, France, 1989, Vol. 1, p. 269.